

**NASA TECHNICAL NOTE**

**NASA TN D-6865**



**NASA TN D-6865**

LOAN COPY: RET  
AFWL (DOU  
KIRTLAND AFB,



**ANALYSIS OF THE FLOW IN  
A 1-MJ ELECTRIC-ARC SHOCK TUNNEL**

*by John O. Reller, Jr., and N. M. Reddy*

*Ames Research Center*

*Moffett Field, Calif. 94035*





0133380

1. Report No. NASA TN D-6865	2. Government Accession No.	3. Recipient's Catalog No.	
4. Title and Subtitle <b>ANALYSIS OF THE FLOW IN A 1-MJ ELECTRIC-ARC SHOCK TUNNEL</b>		5. Report Date <b>June 1972</b>	6. Performing Organization Code
7. Author(s) <b>John O. Reller, Jr., and N. M. Reddy</b>		8. Performing Organization Report No. <b>A-4341</b>	
9. Performing Organization Name and Address <b>NASA—Ames Research Center Moffett Field, Calif. 94035</b>		10. Work Unit No. <b>117-07-04-15-00-21</b>	11. Contract or Grant No.
12. Sponsoring Agency Name and Address <b>National Aeronautics and Space Administration Washington, D. C. 20546</b>		13. Type of Report and Period Covered <b>Technical Note</b>	
15. Supplementary Notes		14. Sponsoring Agency Code	
16. Abstract <p>An investigation has been conducted in the Ames electric-arc-heated shock tunnel to evaluate the performance of the facility over a range of shock Mach numbers from 7 to 19. The efficiency of the arc-heated driver is deduced using a new form of the shock-tube equation. A theoretical and experimental analysis is made of the tailored-interface condition. The free-stream properties in the test section, with nitrogen as the test gas, are evaluated using a method based on stagnation-point heat-transfer measurements.</p>			
17. Key Words (Suggested by Author(s)) <b>Shock tunnels Nozzle flow Arc-discharge heating Calibrating Test facilities</b>	18. Distribution Statement <b>Unclassified — Unlimited</b>		
19. Security Classif. (of this report) <b>Unclassified</b>	20. Security Classif. (of this page) <b>Unclassified</b>	21. No. of Pages <b>28</b>	22. Price* <b>3.00</b>



# TABLE OF CONTENTS

	Page
NOTATION . . . . .	v
SUMMARY . . . . .	1
INTRODUCTION . . . . .	1
THEORETICAL CONSIDERATIONS . . . . .	2
The Shock-Tube Equation . . . . .	2
Driver Efficiency . . . . .	3
Tailored-Interface Operation . . . . .	3
Test Section Flow . . . . .	5
EXPERIMENTS . . . . .	6
The Test Facility . . . . .	7
Driver Performance . . . . .	7
Reservoir Conditions . . . . .	8
Test Section Measurements . . . . .	9
The three-probe rake . . . . .	9
The survey rake . . . . .	10
DISCUSSION . . . . .	11
Nozzle Test Core . . . . .	12
Total Enthalpy . . . . .	12
Free-Stream Properties . . . . .	14
Atom concentration . . . . .	15
Velocity . . . . .	15
Density . . . . .	16
Shock-layer viscosity . . . . .	16
Shock-layer Reynolds number . . . . .	17
Mach number, Reynolds number, and $A/A^*$ . . . . .	17
CONCLUDING REMARKS . . . . .	17
REFERENCES . . . . .	19
TABLES . . . . .	21



## NOTATION

$a$	speed of sound
$A$	constant in equation (21), $A = 6 \times 10^{20} \text{ cm}^3 \text{ }^\circ\text{K/mole sec}$ ; effective area of inviscid nozzle flow
$c_b$	coefficient of specific heat for Pyrex 7740
$d$	diameter
$E$	internal energy
$E_c$	capacitor bank energy
$h_R^0$	heat of dissociation per unit mass
$H$	total enthalpy
$H_R$	reference enthalpy (300 J/g)
$j$	0 for two-dimensional flow; 1 for axisymmetric flow
$K_b$	coefficient of conductivity of Pyrex 7740
$Le$	Lewis number
$m$	molecular weight
$M_s$	shock Mach number ( $U_s/a_1$ )
$p$	pressure
$p_t$	pitot pressure
$Pr$	Prandtl number
$\dot{q}$	convective heat-transfer rate
$R$	gas constant per unit mass of undissociated molecules
$R_n$	dimensionless velocity number defined in equation (1)
$S$	entropy
$S_n$	shock tube number defined in equation (2a)
$T$	absolute temperature
$U$	flow velocity relative to tube wall

$U_s$	shock velocity
$U_3$	limiting velocity, $2a_4/\gamma_4 - 1$
$V$	volume of the driver
$Z$	compressibility, $1 + \alpha$
$\alpha$	atom concentration
$\alpha_p$	temperature coefficient of resistance of platinum film
$\gamma$	ratio of specific heats
$\delta^*$	boundary-layer displacement thickness
$\epsilon$	density ratio across a normal shock wave, $\rho_1/\rho_2$
$\mu$	dynamic viscosity
$\rho$	gas density
$\rho_b$	density of Pyrex 7740
$\eta$	efficiency of the driver
$\psi$	parameter involving $\gamma$ , defined in equation (10)
$\theta$	characteristic dissociation temperature; 113,260° K for nitrogen

#### Subscripts

0	reservoir condition at end of shock tube
1	quiescent test gas ahead of incident shock wave
2	test gas between incident shock wave and contact surface
3	driver gas behind incident contact surface
4	driver chamber conditions after arc discharge
$e$	edge of the boundary layer
$eq$	equilibrium boundary-layer model
$fc$	fully catalytic
$fm$	free molecule flow model
$fr$	frozen boundary-layer model

$i$  initial driver condition before arc discharge

$nc$  noncatalytic

$T$  tailored interface

$\infty$  free-stream condition at exit of nozzle

#### Superscript

\* nozzle sonic throat

# ANALYSIS OF THE FLOW IN A 1-MJ ELECTRIC-ARC SHOCK TUNNEL

John O. Reller, Jr., and N. M. Reddy\*

Ames Research Center

## SUMMARY

An investigation has been conducted in the Ames electric-arc-heated shock tunnel to evaluate the performance of the facility over a range of shock Mach numbers from 7 to 19. The efficiency of the arc-heated driver is deduced using a new form of the shock-tube equation. A theoretical and experimental analysis is made of the tailored-interface condition. The free-stream properties in the test section, with nitrogen as the test gas, are evaluated using a method based on stagnation-point heat-transfer measurements.

## INTRODUCTION

The shock driven wind tunnel has played an important role in the study of hypervelocity aerodynamics, in part because of the wide range of flow velocities available and the relative ease with which the composition of the test stream can be varied. Relatively long duration test flows may be obtained with the tailored-interface mode of operation, as discussed in references 1 and 2. Heated hydrogen drivers (ref. 3) and combustion drivers (refs. 4, 5, 6) have been extensively used to produce tailored shock Mach numbers in the range of 6 to 9. However, higher shock Mach numbers are necessary to dissociate and ionize gases such as nitrogen and carbon monoxide, which are of interest in planetary entry studies. To achieve such conditions within the constraints imposed by the tailored mode of operation requires driver gas temperatures in excess of  $2000^{\circ}$  K. Arc-discharge heating (refs. 7 and 8) has been used successfully in this application; a wide range of driver temperatures is made available by varying driver loading pressure or discharge energy. This attractive scheme has been used for the Ames electric-arc shock tunnel (EAST), which has a capacitor storage system rated at 1 MJ.

In the present study, the characteristics of the heated driver and the tailored-interface operation of the shock tube (with nitrogen) have been considered, both theoretically and experimentally. The major emphasis, however, is on evaluating the properties of the highly expanded nitrogen stream in the test section. In this low-density environment, the more conventional methods of stream evaluation, which rely on probe measurements of static pressure, are inaccurate, largely because of substantial corrections for orifice and probe boundary-layer effects. Thus, in this study a number of quantities characterizing the flow in the EAST test section have been deduced using a new technique based on stagnation-point heating-rate measurements. Other flow properties were obtained from these measurements by application of the sudden-freeze concepts of reference 6. The results are compared with numerical solutions of nonequilibrium nozzle flow using the method of reference 9.

---

\*NASA-NAS Research Associate. Presently at Indian Institute of Science, Bangalore - 12, India.

## THEORETICAL CONSIDERATIONS

The idealized performance of an electric-arc-heated driver and shock tube can be predicted easily for any driver gas or test gas mixture using the generalized form of the classical shock-tube equation presented in reference 10. This form of the shock-tube equation presents simple expressions for the tailored mode of operation and provides an easy method of calculating the actual efficiency of the electric-arc-heated driver. This information is the basis for estimating reservoir conditions at the nozzle inlet for an arbitrary test gas. These conditions in turn are input quantities for calculating the flow properties in the expansion nozzle and test section. The concepts of reference 10 are reviewed briefly and applied to the arc-heated driver; comparisons are made of predicted and realized reservoir conditions.

### The Shock-Tube Equation

It is shown in reference 10 that by defining a dimensionless velocity

$$R_n \equiv \frac{U_2}{\hat{U}_3} \quad (1)$$

the classical shock-tube equation, relating particle velocity behind the incident shock wave to driver gas properties before diaphragm opening, can be reduced to a universal form given by

$$S_n = \frac{(1 - R_n)^{\gamma_4/(\gamma_4 - 1)}}{R_n} \quad (2a)$$

where

$$S_n = \frac{2\gamma_1}{\gamma_4 - 1} \frac{a_4/a_1}{\sqrt{\gamma_1 p_4/p_1}} = \frac{2\gamma_4}{\gamma_4 - 1} \sqrt{\frac{\rho_1/\rho_4}{\gamma_4}} \quad (2b)$$

and

$$R_n = \frac{(\gamma_4 - 1)(1 - \epsilon)M_s}{2(a_4/a_1)} \quad (2c)$$

In equations (2) the driver gas is assumed to be perfect, but no assumption as to the thermodynamic state of the driven gas is made. (Equations (2) are for a constant-area tube and represent the exact solution for perfect gases to within 3 percent at  $M_s > 4$ .)

In an electric-arc-heated facility, the driver gas is heated at constant volume and hence the initial density  $\rho_i$  is equal to the final density  $\rho_a$  after heating. Hence

$$\frac{\rho_1}{\rho_a} = \frac{\rho_1}{\rho_i} \quad (3)$$

Also

$$\frac{\rho_1}{\rho_i} = \frac{p_1}{p_i} \frac{m_1}{m_i} \quad (4)$$

since in general  $T_1 = T_i$ . With the use of equations (3) and (4), the shock-tube equation can be reduced to

$$S_n = \frac{2\gamma_4}{\gamma_4 - 1} \sqrt{\frac{(p_1/p_i)(m_1/m_i)}{\gamma_4}} = \frac{(1 - R_n)^{\gamma_4/(\gamma_4 - 1)}}{R_n} \quad (5)$$

Thus, the dimensionless shock-tube number  $S_n$ , for constant-volume heating of the driver gas, depends only on the initial pressures and molecular weights of the driver and driven gases. Equation (5) is convenient to use for estimates of shock-tube performance for any combination of gases; in graphical form, the variation of  $R_n$  with  $S_n$  is a single curve for a given  $\gamma_4$ . The value of  $R_n$  that corresponds to a particular  $S_n$  is unique in the sense that it is independent of the thermodynamic state of the gas behind the shock wave. Having  $R_n$ , we use equation (2c) to relate  $M_S$  directly to  $a_4$  and  $T_4$ , the speed of sound and temperature in the heated driver gas. Obviously, if  $M_S$  is measured, then an effective  $T_4$  can be determined.

### Driver Efficiency

In an electric-arc-heated driver with constant volume heating of a perfect gas (ref. 11)

$$\frac{T_4}{T_1} = 1 + (\gamma_i - 1) \frac{\eta E_c}{V p_i} \quad (6)$$

and

$$\frac{a_4}{a_1} = \left( \frac{\gamma_4}{\gamma_1} \frac{m_1}{m_i} \frac{T_4}{T_1} \right)^{1/2} \quad (7)$$

These driver-heating equations can be combined with shock tube equations (2c) and (5) to obtain the efficiency of the driver. With  $a_4/a_1$  derived from measured  $M_S$ , and equation (2c) with the appropriate value of  $R_n$ , equation (6) will yield  $\eta$ . In the present study,  $\eta$  was based on  $M_S$  measured at the downstream end of the shock tube, and as such includes losses associated with shock-wave attenuation. It could be reasoned that this approach results in a lower estimated driver efficiency, because it does not account for viscous losses in the shock tube; however, the result does give an estimate of overall driver effectiveness. The efficiencies so determined are discussed in a later section on driver performance.

### Tailored-Interface Operation

At the downstream end of the shock tube a reservoir of heated gas is produced by reflection of the incident shock wave from the end wall. An optimum condition exists if the downstream wave, resulting from the interaction of the reflected shock wave with the contact surface, is a Mach wave. When this occurs, the contact surface (interface) is said to be "tailored." Since this secondary reflection is vanishingly weak, the reservoir conditions remain steady for a longer period — in theory, until the arrival of the main driver expansion. For tailored operation a matching condition can be derived for the perfect driver and driven gas case, as shown in reference 12; for example,

$$\left[ \frac{E_3}{E_2} \right]_T \approx \frac{\gamma_4 + 1}{\gamma_4 - 1} \frac{\gamma_1 - 1}{\gamma_1 + 1} \quad M_s^2 \gg 1 \quad (8)$$

The dimensionless number  $R_n$  can be used to write the ratio of internal energies, following reference 10, as

$$\frac{E_3}{E_2} = \frac{\gamma_4 - 1}{2\gamma_4} \left( \frac{1 - R_n}{R_n} \right)^2 \quad (9)$$

From equations (8) and (9) the tailored value of  $R_n$  is

$$[R_n]_T = \frac{1}{1 + \psi^{1/2}} \quad (10)$$

where

$$\psi = \frac{\gamma_4 + 1}{\gamma_4 - 1} \frac{2\gamma_4}{\gamma_4 - 1} \frac{\gamma_1 - 1}{\gamma_1 + 1}$$

Then equation (5) reduces to

$$[S_n]_T = \frac{2\gamma_4}{\gamma_4 - 1} \left[ \frac{m_1/m_i}{\gamma_4(p_i/p_1)} \right]^{1/2} = \frac{\psi^{\gamma_4/2(\gamma_4-1)}}{(1 + \psi^{1/2})^{1/(\gamma_4-1)}} \quad (11)$$

Equations (10) and (11) represent the tailoring conditions for thermodynamically perfect gases. From equation (11) it is evident that for a given combination of driver and driven gases, the ideal loading pressure ratio  $p_i/p_1$  required for tailored operation is a constant, regardless of the quantity of energy discharged into the driver gas. The loading pressure ratios for tailored operation with the different gas combinations used in these experiments are given in table 1.

The tailored shock Mach number is given by

$$[M_s]_T = \frac{2(a_4/a_1)}{(\gamma_4 - 1)(1 - \epsilon)} [R_n]_T \quad (12)$$

Using equations (6) and (7) to obtain  $a_4/a_1$ , equation (12) can be written as

$$[M_s]_T = [R_n]_T \frac{2}{(\gamma_4 - 1)(1 - \epsilon)} \left\{ \frac{\gamma_4}{\gamma_1} \frac{m_1}{m_i} \left[ 1 + (\gamma_4 - 1) \frac{\eta E_C}{V p_i} \right] \right\}^{1/2} \quad (13)$$

where  $\epsilon \approx (\gamma_1 - 1)/(\gamma_1 + 1)$  is the perfect gas value of the density ratio across a normal shock wave for  $M_s \gg 1$ , and  $[R_n]_T$  is the constant given by equation (10). The tailored shock Mach number  $[M_s]_T$  depends on the initial loading pressure  $p_i$ , the driver volume  $V$ , the stored capacitor energy  $E_C$ , and the choice of gases. A typical variation of  $[M_s]_T$  with  $p_1$ , with He driving  $N_2$ , is given in figure 1, for  $E_C = 10^6$  J and  $V = 0.0209$  m<sup>3</sup> (Ames 2.90 m arc-heated driver). As shown, this result from equation (13) compares favorably with a similar result from reference 2 where, for the same He-N<sub>2</sub> combination, nitrogen is treated as a real gas.

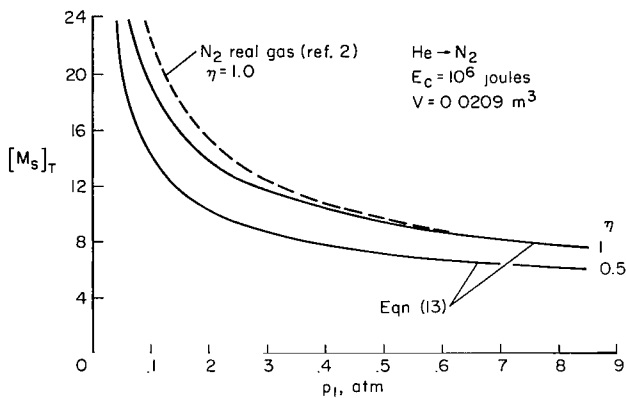


Figure 1.— Variation of tailored-shock Mach number with shock-tube loading pressure.

impossible to predict from ideal theory the ratio of pressures that will give a tailored condition. However, a near-tailored reservoir can be obtained by adjusting  $p_i$  and  $p_1$ , as discussed later.

The preceding analysis indicates that if the appropriate ratio of  $p_i$  to  $p_1$  is chosen the contact surface will be tailored at all shock Mach numbers. With the assumption of ideal shock-tube theory with thermodynamically perfect working gases inherent to this analysis, each tailored shock Mach number has a unique ratio of temperatures across the contact surface ( $T_3/T_2$ ). In practice, this is not the case, however, because the temperature  $T_3$  is influenced by real-gas effects, viscous losses, heat transfer to the wall, and nonuniform distribution of energy within the driver chamber. The temperature  $T_2$  is affected by similar viscous and heating losses, real-gas effects, diaphragm opening, etc. Thus, these nonideal effects make it

### Test Section Flow

This section considers methods of evaluating flow properties in the high-velocity test stream issuing from a steady reservoir of quiescent, shock-heated gas. It is assumed that the reservoir gas is in equilibrium, with respect to both vibrational and chemical energies. In reference 13 a method is described for determining the Reynolds number, viscosity, and atom concentration in a hypervelocity nozzle from the measurement of stagnation-point heat-transfer rates to three probes placed side by side (the three-probe method). The physical nose dimensions of the probes should be chosen so that one probe measures the heating rate  $\dot{q}_{eq}$  in the presence of an equilibrium (chemical) boundary layer, the second  $\dot{q}_{fr}$  in a frozen shock layer, and the third  $\dot{q}_{fm}$  in the free-molecule flow regime. With a pitot-pressure measurement, in addition to these three heating rates, the following relationships can be used. (The derivation of these equations and the probe design considerations are given in reference 13. The present results are subject, of course, to the assumptions of the reference analysis.) The shock-layer Reynolds number is

$$(Re)_e \equiv \frac{\rho_\infty U_\infty d_{fr}}{2\mu_e} = C^2 \left( \frac{\dot{q}_{fm}}{\dot{q}_{fr}} \right)^2 \quad (14)$$

where

$$C = 0.64(j+1)^{1/2} Pr^{-0.6} e^{-0.25}$$

The ratio of dissociation to total enthalpy is

$$\frac{\alpha_\infty h_R^0}{H_\infty} = \frac{\dot{q}_{eq} d_{eq}^{1/2} - \dot{q}_{fr} d_{fr}^{1/2}}{\dot{q}_{eq} d_{eq}^{1/2} + (Le^{0.52} - 1) \dot{q}_{fr} d_{fr}^{1/2}} \quad (15)$$

In equation (15) the two heat-transfer probes are assumed to be geometrically similar. Using the approximations

$$p_t \approx \rho_\infty U_\infty^2 \quad \text{and} \quad H_\infty \approx \frac{1}{2} U_\infty^2 + h_R^o \alpha_\infty$$

one obtains

$$U_\infty = \frac{2\dot{q}_{fm}}{p_t} \quad (16)$$

$$\rho_\infty = \frac{p_t^3}{4\dot{q}_{fm}^2} \quad (17)$$

$$\mu_e = \frac{1}{4} \frac{d_{fr}}{C^2} \frac{p_t^2 \dot{q}_{fr}^2}{\dot{q}_{fm}^3} \quad (18)$$

$$H_\infty = \frac{U_\infty^2}{2Le^{0.52}} \left[ \frac{\dot{q}_{eq} d_{eq}^{1/2}}{\dot{q}_{fr} d_{fr}^{1/2}} + (Le^{0.52} - 1) \right] \quad (19)$$

$$\alpha_\infty = \frac{U_\infty^2}{2h_R^o Le^{0.52}} \left( \frac{\dot{q}_{eq} d_{eq}^{1/2}}{\dot{q}_{fr} d_{fr}^{1/2}} - 1 \right) \quad (20)$$

All the flow properties in the preceding equations are expressed in terms of the measured quantities, stagnation heating rate and pitot pressure. The unknowns are the two transport properties, Lewis and Prandtl numbers, and the shock density ratio  $\epsilon$ , which must come from another source. Fortunately, they are relatively insensitive to test conditions and can be matched by an iterative solution if desired. An examination of equations (14) through (20) shows that the derived values of free-stream velocity  $U_\infty$ , density  $\rho_\infty$ , shock-layer viscosity  $\mu_e$ , and Reynolds number  $[Re]_e$  require only two of the three measured heating rates, namely  $\dot{q}_{fr}$  and  $\dot{q}_{fm}$ ; and that the free-stream Mach number  $M_\infty$  and Reynolds number  $Re_\infty$  cannot be obtained by this method, since the static temperature of the stream is not directly available. However, these latter properties can be derived from the present measurements by an adaptation of the sudden-freeze method of reference 6, as will be shown later. To assess the validity of this combined approach, a comparison will be made between the stream densities from the three-probe and the sudden-freeze methods, while  $U_\infty$  from equation (16) will be compared to the stream velocity obtained by a completely independent analysis.

## EXPERIMENTS

In this section the methods discussed for determining driver efficiency, tailored-interface conditions, and flow properties are applied to the EAST facility.

## The Test Facility

An electric-arc driver and energy storage system has been developed for shock-tunnel application, with provision for driver lengths up to 3 m. Such driver lengths are required to match the reservoir time requirements for tailored-interface operation (ref. 2). The energy for the arc is supplied by a 1250- $\mu$ F capacitor bank capable of storing 1 million joules when charged to a maximum of 40 kV. The arc is contained within a 10.2-cm-diam insulated chamber and is initiated by a tungsten wire. Details of the operating characteristics for the driver system are given in reference 14. (Dannenberg and Silva have developed methods to improve driver performance and range of operation; these are described in a forthcoming publication.) For the present experiments, driver lengths of 1.37 and 2.90 m were used. The energy per unit volume  $E_C/V$  was kept the same for both lengths (about 42 J/cm<sup>3</sup>) with capacitor bank voltages of 28 and 40 kV, respectively. The driver is coupled to a 10.2-cm-diam, 11.3-m-long shock tube, which discharges into a 10° half angle, conical supersonic nozzle. A 76-cm, hexagonal test section and a vacuum tank are located downstream of the nozzle. Figure 2 is a schematic diagram of the facility. Interchangeable sonic

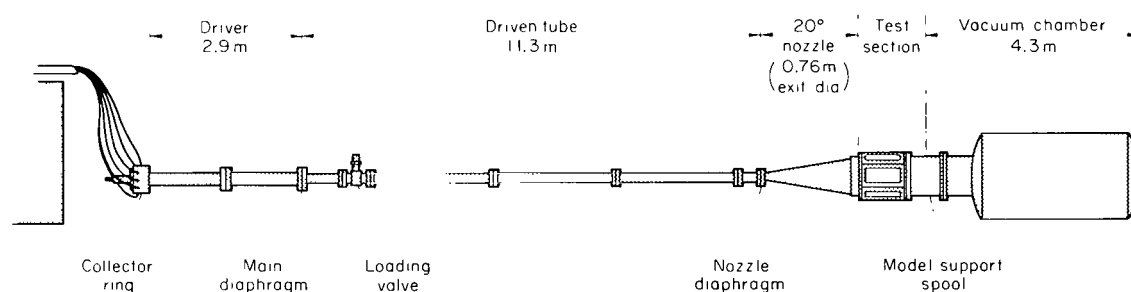


Figure 2.— Schematic of Ames electric-arc shock tunnel.

throats can be inserted at the nozzle entrance to permit operation at different flow Mach numbers. The shock wave arrival was monitored at six stations in the shock tube using the ion-probe system described in reference 15. Shock Mach number was calculated from the measured velocity and the initial gas temperature in the tube. The initial pressure  $p_1$  was measured with a precision dial gage at the gas loading station, and the reservoir pressure  $p_0$  with a piezoelectric transducer located in a sidewall port at 0.64 cm from the endwall. Test gas impurities were estimated to be less than  $1.0 \times 10^{-3}$  of the total sample.

## Driver Performance

Driver efficiencies, determined by the method described earlier, are shown in figure 3 for the range of loading pressures  $p_i$  of the present tests. Equivalent driver temperatures computed from equation (6) are included for reference. Experimentally determined efficiencies were based on the shock velocity measured near the end of the 11.3-m tube and thus include the energy loss associated with shock attenuation. At values of  $p_i$  from 10 to 15 atm, the He and N<sub>2</sub> drivers operate with an overall efficiency of about 50 percent. With the addition of argon to the driver gas, which lowers  $M_S$  because of the decrease in  $a_4$ , the driver efficiency varied substantially from run to run. In all cases  $\eta$  was better than for helium alone, but the wide variation from 0.60 to over 1.0 is a surprising result. It is inferred that the arc-discharge and heat-transfer processes in the driver chamber are variable, perhaps because of local variations in gas mixture ratio. Since the basis of comparison is a

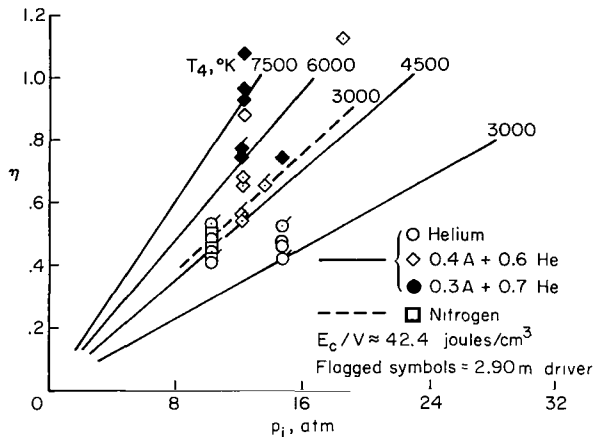


Figure 3.— Overall driver efficiency and equivalent temperature; 1.37- and 2.90-m drivers.

### Reservoir Conditions

In an earlier section, the ratios of initial driver-to-driven-tube pressures were predicted for tailored interface operation with ideal gases. For a given combination of gases the ratio is a fixed constant, although absolute values can be changed to vary  $M_S$ . As part of the experiment, an effort was made to validate this prediction, using the pressure ratios listed in table 1. It was quickly found that nonideal effects resulted in undertailored conditions — an undertailored condition is a mismatch of internal energy at the contact surface such that  $E_3 > E_2$ , causing a downstream expansion wave to emerge from the reflected shock-contact surface interaction. This situation can be corrected by lowering  $p_1$ , while keeping  $a_4/a_1$  constant, or by decreasing  $a_4/a_1$  with  $p_1$  constant, until the tailored condition is achieved. To obtain reasonably constant reservoir pressure histories with nitrogen as the test gas, it was necessary to increase the ratios  $p_i/p_1$  by about an order of magnitude by a reduction in  $p_1$ . This is not surprising since the shock Mach numbers attained in most high-energy shock tubes are below ideal predictions at the initial pressures considered here. The observed departure from the ideal pressure ratio in this experiment is attributed to an elevated temperature behind the contact surface  $T_3$ , partly due to deceleration of the incident shock wave and partly to a timewise variation of total temperature in the gas issuing from the driver. These nonideal effects are the subject of a separate investigation.

Figure 4 shows representative reservoir pressure histories for the  $M_S$  range and the driver gases used. Figure 4(a) is a record of a somewhat undertailored condition at  $M_S = 18.5$ , which has a fairly constant pressure after the arrival of the expansion wave from the contact surface. This pressure level corresponds to an enthalpy in the test gas of about 40 kJ/g, considerably above that obtainable in combustion or heated hydrogen driven facilities. The tailored condition would occur at a slightly lower  $p_1$  for  $M_S > 18.5$ . Figures 4(b) and 4(c) show slightly overtailored conditions for which weak compression waves augment the reflected-shock pressure.

An independent check of the reservoir gas quality was obtained by monitoring the radiant emission of the shock-heated nitrogen, using a photodiode detector with S-1 response. The reservoir gas was observed through a sidewall window masked by a 0.025-cm vertical slit for collimation; signals were recorded on an oscilloscope. Although the detector was not calibrated for absolute intensity, care was taken to operate in the linear response range. Typical results (fig. 5) show that

uniformly heated driver gas, it is obvious that nonideal effects can be strong enough to create shock waves that exceed the ideal velocity. It should be noted, moreover, that  $\eta > 1.0$  has been reported in reference 8 for pure helium drivers at relatively low temperatures  $T_4$ . Here again one logical explanation is nonuniform driver heating. Further investigation of this behavior is warranted since it will influence interface temperatures  $T_2$  and  $T_3$ , which determine tailored operation.

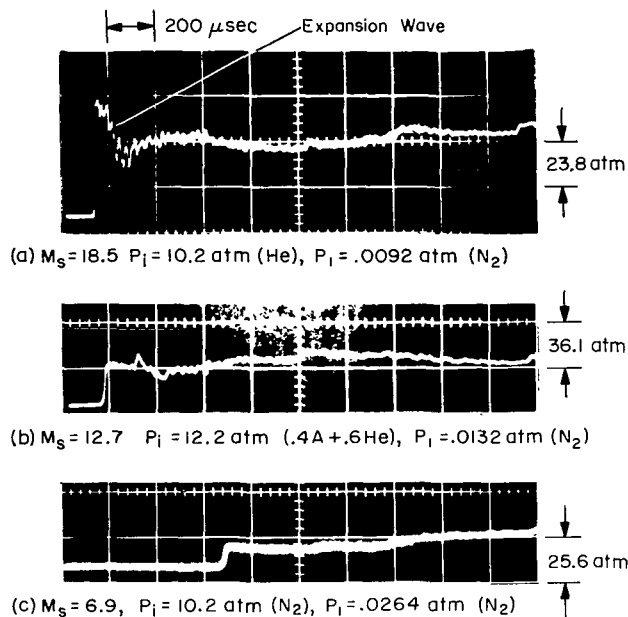


Figure 4.— Reservoir pressure histories at near-tailored conditions.

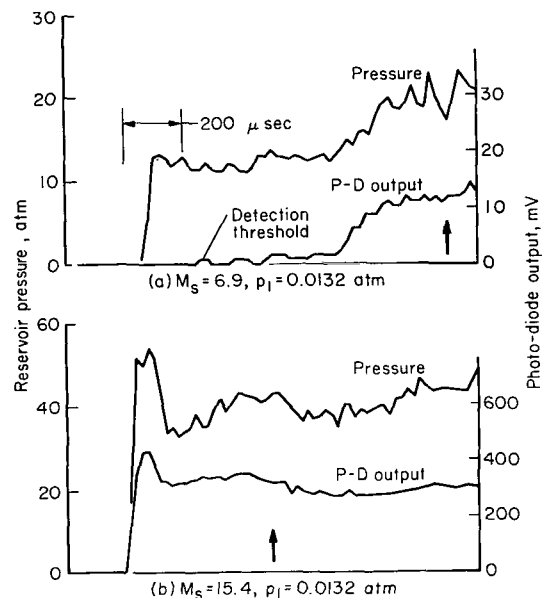


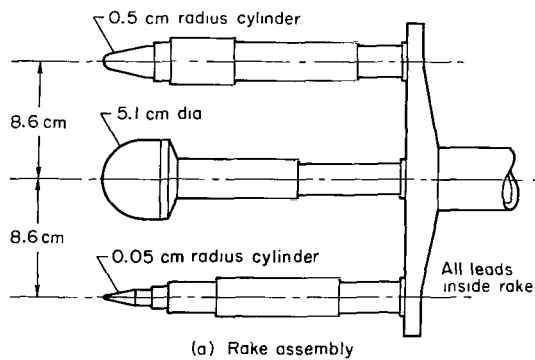
Figure 5.— Pressure and radiation histories in the reservoir, 0.64 cm from end wall.

the radiation from the reservoir varies with the pressure for at least 1 msec at  $M_S = 6.9$ , and for about 0.5 msec at  $M_S = 15.4$ . In a qualitative sense, this finding indicates that no large dilution of the test gas occurs in these times.

### Test Section Measurements

As the shock-heated, partly dissociated nitrogen in the reservoir expands into and beyond the throat of the supersonic nozzle, a point is reached where the recombination and vibrational relaxation become rate limited and can no longer follow the rapid change of temperature. When this occurs, the flow changes over a relatively short distance from local equilibrium to a state in which one or both of the two forms of internal energy (vibration and dissociation) are nearly invariant. In effect, the flow “freezes” at an intermediate level of dissociation and vibrational energy distribution, and remains essentially in this state as it sweeps through the test section. Consequently, the properties of the test stream differ from those in an equilibrium expansion; the temperature, pressure, and velocity are lower while the Mach number is higher. The calibration method must determine these differences, measure the dissociation level, and if possible, the vibrational energy defect of the flow.

*The three-probe rake*— The flow quantities in the test section were evaluated, in part, using the three-probe method described earlier. The probes were mounted together on a single rake for simultaneous measurements of stagnation-point heating rates in the equilibrium boundary layer, frozen shock layer, and free-molecule flow regimes. The nose diameters were  $d_{eq} = 5.1$  cm,  $d_{fr} = 1.0$  cm, and  $d_{fm} = 0.10$  cm; the largest probe was hemispherical and the two smaller probes were cylindrical in shape. Figure 6 shows a diagram and a photograph of the three-probe rake immersed in the test flow. For the present range of conditions, the computations presented in reference 13 show that a cylindrical probe of 0.10 cm diam is sufficiently small to obtain



(b) Rake in test stream

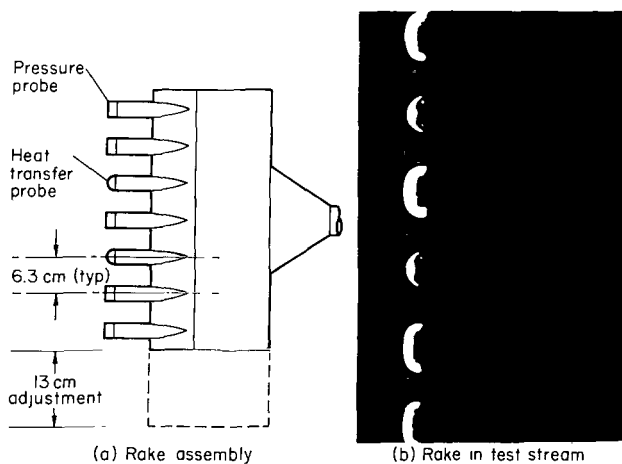
Figure 6.— Three-probe heat-transfer rake.

The sensing elements on the three probes were thin film platinum gages. To avoid shorting due to shock-layer ionization, all the gages were coated with a  $1\text{-}\mu$ -thick layer of silicon monoxide by a vacuum evaporation technique. (The response time of a  $1\text{-}\mu$  glass layer is about  $50\ \mu\text{sec}$  for 5 percent accuracy.) The backing material used was Pyrex 7740, which has the following properties:  $(K_b \rho_b c_b)^{1/2} = 0.153\ \text{J cm}^{-2}\ \text{°K}^{-1}\ \text{sec}^{-1/2}$  and  $\alpha_p = 2.18 \times 10^{-3}\ \Omega/\Omega\ \text{°K}$ . The heat-transfer rates

free-molecule flow at the stagnation point. On the basis of estimates and experimental results presented in reference 16, a cylindrical probe of 1.0-cm diam should result in frozen shock-layer conditions.

Estimates of the probe size for equilibrium boundary-layer flow in the stagnation region were based on the theory of reference 17. Although the reference analysis is specifically for air, it was assumed that the functional dependence of gas-phase reactions on local conditions would be similar for pure nitrogen. The resulting estimates of probe size, in the limit of a fully equilibrium boundary layer, exceeded the physical dimensions of the facility for many of the expected test conditions. Therefore, it was decided to relax the requirement of full equilibrium, retain the concept of three simultaneous measurements, and resolve the defect in heating rate by analytical means. A 5.1-cm-diam hemisphere was used for this measurement; for convenience, this probe will be referred to as the equilibrium heat-transfer probe.

were determined directly with the use of analog networks. The methods of reference 16 were followed closely in the design and construction of both the gages and the analog networks.



(a) Rake assembly

(b) Rake in test stream

Figure 7.— Pressure and heat-transfer survey rake.

*The survey rake*— During test core surveys, other heating rates were measured on hemispherical models 2.5 cm in diam mounted on a rake spanning the test region (fig. 7). These models were copper shells, 0.013 cm thick, instrumented with 40 gage chromel-constantan thermocouples formed by soldering the individual wires of each pair into two closely spaced holes at the stagnation point. All the heat-transfer data were recorded by a high-speed data acquisition system (ref. 18), which provides digital information at the rate of one reading

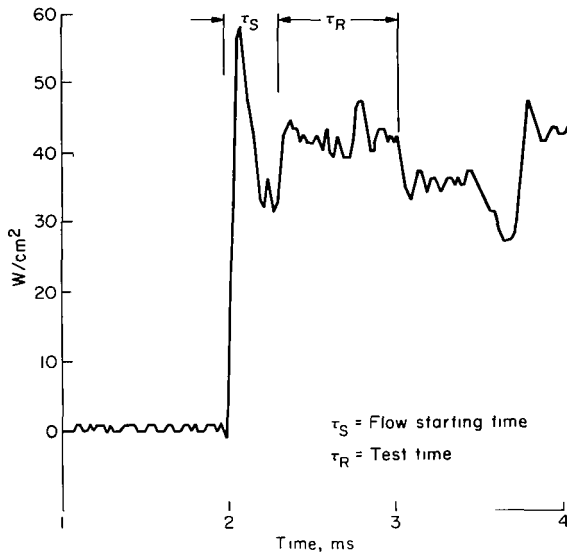


Figure 8.— Rate of heat transfer to the equilibrium boundary-layer probe ( $M_S = 12.4$ ,  $p_i = 0.0132$  atm).

heat-sink baffle to shield the active element (a pretensioned Invar diaphragm, 0.0013 cm thick) from heating effects.

The heat-transfer rates and the corresponding pitot pressures were measured for a wide range of shock Mach numbers (hence reservoir enthalpies) with nitrogen as the test gas. The driver gases were nitrogen, pure helium, and helium diluted with different amounts of argon; for each case the ratio of initial driver pressure to driven tube pressure  $p_i/p_1$  was adjusted until a near-tailored condition was achieved. The three-probe rake was mounted in the horizontal center plane at the exit of a conical supersonic nozzle with a 0.32-cm-diam throat. The pressure and heat-transfer survey rake was mounted vertically in the same nozzle, at the same axial station, and offset to position pitot probes at the same radial distance as the outer models on the three-probe rake. Throat sizes of 0.32 and 1.27 cm were used with this rake. For the present range of experiments, the corrections to measured pitot pressures for rarefaction effects were estimated by the method of reference 19 and found to be less than 2 percent. The flow starting time in the nozzle (as in ref. 20, the time required to establish uniform flow after arrival of initial disturbance) is estimated from probe response to be between 150 to 300  $\mu\text{sec}$ , and in general, varies inversely with  $M_S$ .

## DISCUSSION

The data are summarized in table 2; the measured heating rates, pressures, and test times are grouped into two sets according to the instruments used. Test 1 refers to the runs made with the three-probe heat-transfer rake, using thin-film detectors. Test 2 results are from the survey rake that used thin-wall calorimeters to measure heat-transfer rates and variable capacitance transducers for pressure.

Analysis of the heat-transfer data from three-probe rake (test 1) gave inconsistent results over the range of test conditions. To isolate the cause of this erratic behavior, test 2 repeated several runs

every 2  $\mu\text{sec}$ . The data were punched on a paper tape and processed on an IBM 7094 computer. A sample of the machine-plotted heat-transfer data is shown in figure 8.

Pitot pressures were measured, in repeat runs at each test condition, with a piezoelectric pressure transducer (Kistler, model 701A). These measurements were obtained with both a flush mounting (gage face exposed to the flow) and a recessed mounting arrangement. In both cases the gage face was coated with a very thin layer of silicone rubber to reduce the heating effects. (Reservoir pressures were measured with similar transducers (Kistler, model 601H).) Pitot pressures were also measured during test core surveys with an adjustable rake, which contained as many as seven variable-capacitance pressure transducers. These gages were mounted behind a

at identical starting conditions and extended the scope to include a larger nozzle throat size,  $d^* = 1.27$  cm. Furthermore, as a check on the measuring techniques of test 1, a different type of heat-transfer sensor and pressure transducer were used. These were mounted in the survey rake that spanned the test region. The results of test 2 showed that the inviscid test core was smaller than predicted at the higher reservoir enthalpies. This result can be seen in table 2 where, for test 1, columns 7 and 10 indicate when the pitot pressure at the off-centerline location of the frozen-flow and free-molecule probes was lower than centerline pitot pressure. Column 13 of table 2 lists the time interval of useful data for each run, while column 14 gives an estimate of the duration of test gas flow based on reservoir radiation and test section heating rate measurements. In general, the longer flow times of column 14 could not be fully utilized because of pressure disturbances in the reservoir.

### Nozzle Test Core

Rake surveys of the nozzle flow at the exit station, using the 0.32-cm-diam throat, showed that inviscid test cores varied in diameter from about 23 to 10 cm as the total enthalpy was increased from 8 to 40 kJ/g. Pressures were relatively constant across the core area and repeatable from run to run. At  $H_\infty > 27$  kJ/g, the stream core size decreased to the point where the outer two probes on the heat-transfer rake (located 8.4 cm from the centerline) were in the outer edge of the nozzle wall boundary layer. For these conditions, the frozen-flow probe data were discarded, but the free-molecule probe results were assumed to represent a velocity close to the inviscid core value, since in the outer edge of a hypersonic boundary layer the density decreases much more rapidly than the velocity. For example, for the first run listed in table 2 the local pitot pressure was about 0.7 the centerline value; the corresponding defect in velocity is estimated to be less than 1 percent, while the local density decrease is nearly 30 percent. The corresponding local Mach number is only about 15 percent lower, so that the free-molecule probe should remain within the appropriate flow regime.

With a nozzle throat diameter of 1.27 cm, the measured test core diameter was greater than 40 cm over the entire range of reservoir conditions.

### Total Enthalpy

As shown in table 2, the stagnation region boundary layer on the largest probe, as expected, did not come to chemical equilibrium. Therefore, it was not possible to compute the stream total enthalpy directly using equation (19). An alternate method was devised for indirect verification of the enthalpy, using the measured  $\dot{q}_{fm}$  and  $\dot{q}_{fr}$  along with an  $H_o$  derived from reflected shock conditions. The first step in this approach was to determine the chemical state of the shock layer by comparing the product of the rate of nitrogen dissociation and the flow residence time to the limiting value of equilibrium dissociation. The dissociation rate was estimated using the characteristic equation, as given for example in reference 21, which describes a diatomic gas with a binary collision mechanism

$$\frac{d\alpha}{dt} = (1 - \alpha) \frac{AP}{RT^{1+\omega}} e^{-\theta/T} \quad (21)$$

where  $\omega = 1.5$  is half the number of degrees of freedom contributing energy during a collision and  $A$  is a constant determined by experiment for a particular gas. In the present case  $d\alpha/dt$  was maximized by using the ideal gas ( $\alpha = 0$ ) temperature just behind the shock wave.

Residence time was estimated from shock detachment distance and average local velocity. The uniform result was that even for this *maximum* dissociation rate the residence time was so short that the inviscid shock layer was effectively frozen at the stream composition (on the largest model) for all test conditions. Similarly, for the stagnation region boundary layer, a recombination rate parameter (the ratio of atom diffusion time across the boundary layer to characteristic atom lifetime)

$$C_1 = \frac{1.6 \times 10^{11} pd}{2T^4 Z^{1/2}} \quad (22)$$

was used after the manner of reference 22, with pressure in atmospheres and nose diameter in centimeters. Values of  $C_1$  varied from  $10^{-6}$  to  $10^{-8}$  over the test range and indicate atom lifetimes much in excess of transit time. Thus, the boundary layer in the stagnation region of the 5.1-cm probe is frozen to atom recombination for all test conditions.

With the chemical composition of the probe shock layer thus defined (frozen at stream composition) and assuming that reservoir enthalpy can be evaluated from the measured reservoir pressure at the entropy level associated with the reflected shock wave, the second step is to compute the convective heat transfer to a noncatalytic (glass covered) surface for several assumed values of  $\alpha_\infty$ . When the expression for a frozen free stream and frozen shock layer is used (ref. 22),

$$\dot{q}_{nc} = \dot{q}_{fc} \left( 1 - \frac{\alpha_\infty h_R^0}{H_0} \right) \quad (23)$$

where the heating rate to a fully catalytic surface  $\dot{q}_{fc}$  is essentially the same as that for an equilibrium boundary layer  $\dot{q}_{eq}$ . As suggested in reference 22, this latter value can be closely approximated for nitrogen by

$$\dot{q}_{eq} = 78.8 \left( \frac{2p_t}{d} \right)^{1/2} \left( \frac{\bar{U}_\infty}{10,000} \right)^{2.03} \left( 1 - \frac{H_R}{H_\infty} \right) \quad (24)$$

where  $\bar{U}_\infty \equiv (2H_\infty)^{1/2}$ , the flow velocity for an equilibrium expansion; that is,  $\bar{U}_\infty$  includes the dissociation energy. The resulting values of  $\dot{q}_{nc}$  were interpolated to match the measured heating rate on the 5.1-cm probe, which yields  $\alpha_\infty$  and the corresponding stream velocity  $U_\infty$ .

Alternately,  $U_\infty$  can be computed from equation (16) using the measured data for each test condition

$$U_\infty = \frac{2\dot{q}_{fm}}{p_t} \quad (16)$$

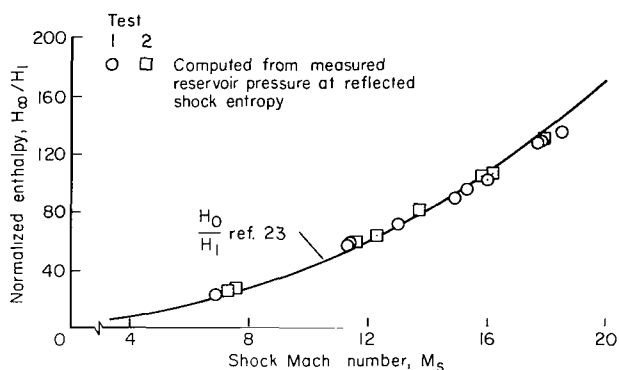


Figure 9.— Variation of total enthalpy with  $M_S$  for nitrogen.

The results of this analysis are shown in table 3, where the two sets of  $U_\infty$  are seen to be in good agreement. This finding implies that there are no significant energy losses in the reservoir for the range of conditions tested, and that the total enthalpy of the test core matches that of the reservoir.

The variation of total enthalpy with  $M_S$  is shown in figure 9. Symbols denote computed values based on the measured reservoir pressure and the entropy level associated with the reflected shock wave. Computed enthalpies are compared with a theoretical, reflected shock curve taken from reference 23; differences are due to the change of reservoir pressure after shock reflection.

### Free-Stream Properties

A nonequilibrium nozzle flow program similar to that of reference 9 was used for comparing the measured flow properties with theoretical predictions. The major uncertainty involved in this program lies in the assumption that the vibrational energy mode always remains in equilibrium with translational and rotational modes. (While the energy in vibrations is at most about 20 percent of the total enthalpy, its disposition can make a noticeable difference in stream properties, as will be shown later.) The reservoir temperature and pressure are specified as initial values for the numerical solution. In the present cases the initial values were the measured reservoir pressure and the corresponding equilibrium temperature obtained from thermodynamic charts for nitrogen, using the appropriate reservoir enthalpy. Energy losses from the reservoir gas were assumed to be negligible; thus, the computed quantities represent a limiting set for the entropy associated with each test condition. The numerical computations showed that the nitrogen atom concentration was frozen in the test section for all the cases considered.

The semiempirical method of reference 6 also can be used to predict certain stream properties, without knowledge of the specific relaxation processes or rate constants. It is assumed that the gasdynamic properties at the test station (having undergone relaxation of several internal degrees of freedom) are approximately the same as if the gas had made a sudden transition from equilibrium to a zero rate of internal energy exchange at some location in the expansion. The location of the transition is characterized by a single parameter, the freeze Mach number. Downstream of this point both the chemical composition and vibrational energy distribution of the gas are constant (frozen).

A computing program for one-dimensional nozzle flow, using equilibrium reservoir conditions as input quantities, was used to generate stream properties as a function of area ratio for a specified set of freeze Mach numbers. The pitot pressure was calculated assuming the vibrational mode and chemistry remained frozen behind the bow shock wave — a realistic choice for the flow conditions of the present experiment. The details and an experimental verification of this method are given in reference 6.

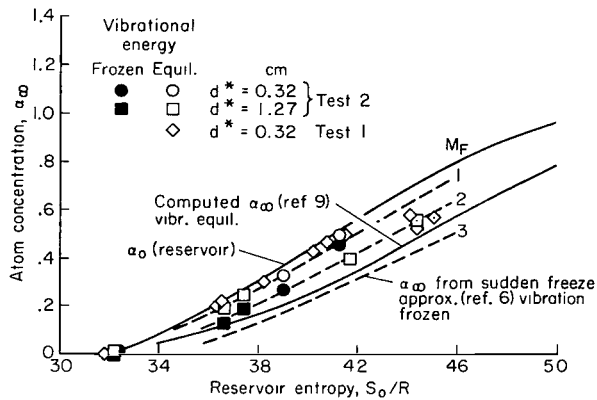


Figure 10.— Free-stream atom concentration.

The filled symbols in figure 10 represent a similar analysis in which both vibrational and chemical energy exchanges become inactive simultaneously in the nozzle expansion and remain so in the probe shock layer. Comparisons of shock-layer residence time with vibrational relaxation rates showed this a reasonable assumption except at the highest enthalpy conditions. Tables 4 and 5 summarize reservoir conditions, stream atom concentrations, and other flow quantities.

The results of figure 10 indicate that a relatively small amount of recombination occurs in the expanding nitrogen flow over most of the operating range, and that the numerical solution (with vibrational equilibrium) substantially underestimates the stream atom concentration. For frozen vibrations, the sudden-freeze approximation indicates that the internal energy adjustment stops just downstream of the nozzle throat, between  $M_\infty = 1$  and 2. The effect of nozzle throat size on atom concentration appears relatively minor over the test range. At  $S_0/R > 42$ , recombination is enhanced and  $\alpha_\infty$  approaches the numerical prediction.

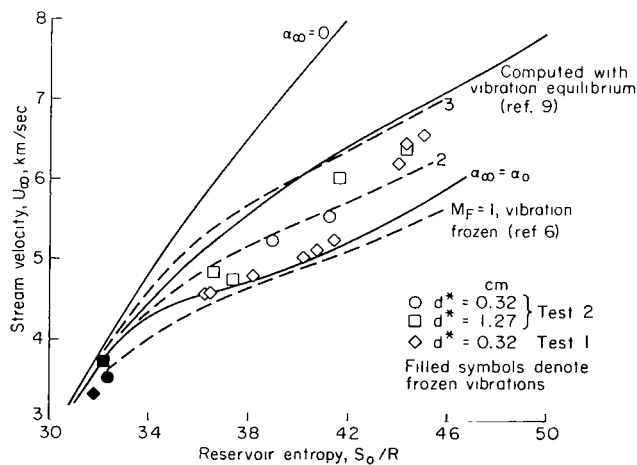


Figure 1.— Comparison of measured and predicted stream velocity.

*Atom concentration*— The measured and computed values of  $\alpha_\infty$  are compared in figure 10 as a function of reservoir entropy. Reservoir atom concentration  $\alpha_0$  is common to both theory and experiment. The open symbols represent concentrations deduced from measured heat transfer, using equations (23) and (24) as described earlier, with vibrational energy assumed to be in equilibrium. For test 2 the probe surface was partly catalytic (copper oxide), and allowance was made for surface recombination by the method of reference 24. The recombination energy fraction varied from 4 to 26 percent of the available dissociation energy.

*Velocity*— Experimental and predicted free-stream velocities are compared in figure 11. The sudden-freeze predictions are shown as dashed lines, shifted downward slightly relative to the numerical solution and the  $\alpha_0$  curve to account for the frozen vibrational energy. The experimental values are consistent with the atom concentrations of figure 10 and, as expected, are substantially lower than the numerical prediction. At the lowest values of  $S_0/R$  the data fall below the curve for  $\alpha_\infty = \alpha_0$  because of frozen vibrational energy. At the higher values of  $S_0/R$ , the velocities move toward the numerical prediction.

In the present analysis, the flow velocity was derived from experimental measurements in two ways: (1) using the stagnation heating rate

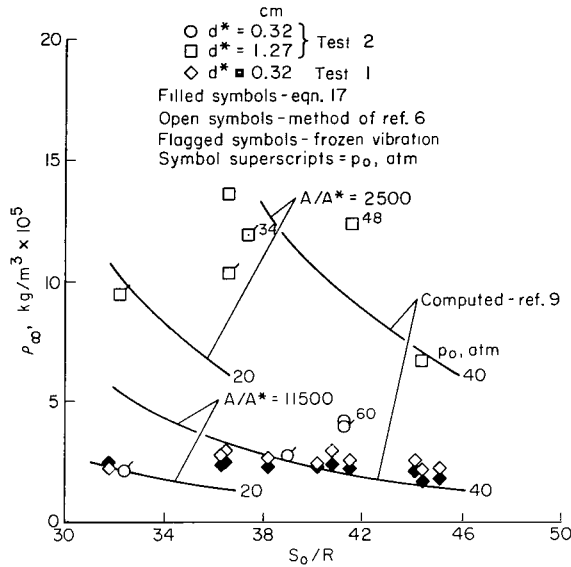


Figure 12.-- Free-stream density.

experimental results agree in general with predictions on this summary plot; more exact comparisons would require a point-by-point analysis since  $\rho_\infty$  is sensitive to both reservoir pressure and local area ratio. (The area ratios shown are average values for each  $d^*$  as determined from the sudden-freeze analysis, while  $p_0$  is within 10 percent of experiment except for the symbols with superscript values. For more detail see tables 4 and 5). The results for test 1, using the sudden-freeze analysis, compare favorably with the more direct values from equation (17). This agreement between stream densities appears to justify the assumption that the sudden-freeze analysis can be used to supplement the stream properties obtained by the three-probe method.

*Shock-layer viscosity*— The viscosity in the stagnation-region shock layer is obtained from the relationship of pitot pressure and heating rates given in equation (18)

$$\mu_e = \frac{d_{fr}}{4C^2} \frac{p_t^2 \dot{q}_{fr}^2}{\dot{q}_{fm}^3} \quad (18)$$

where

$$C = 0.64(j + 1)^{1/2} p_r^{-0.6} \epsilon^{-0.25}$$

The density ratio across the bow shock  $\epsilon$  was evaluated using either  $\gamma = (8 + )/(8 - )$  for equilibrium vibrations, or  $\gamma = (4 + 3)/(4 + )$  for frozen, in the normal shock relation  $\rho_\infty/\rho_e \approx (\gamma - 1)/(\gamma + 1)$  for  $M_\infty \gg 1$ . A Prandtl number of 0.7 was used throughout. The results are listed in table 4, where the values are seen to increase with  $H_0$  in a regular manner. As a check on the magnitude of these values, equation (A4) of reference 24 was used to determine the shock-layer temperature  $T_e$ . Figure 13 shows that the resulting temperatures exceed the estimated values for dissociated flow with equilibrium vibrational energy; thus the measured viscosities appear consistent with the other findings of this investigation.

for a frozen shock layer, and (2) using the free-molecule heating rate as in equation (16). Comparisons are given in table 3. The first method requires a prior knowledge of the stream total enthalpy; the second does not. For this reason, the  $\dot{q}_{fm}$  method is preferable and, in fact, is a relatively simple way to determine the velocity of a nonequilibrium stream. For best accuracy, both  $\dot{q}_{fm}$  and  $p_t$  should be measured simultaneously.

*Density*— The computed and measured stream densities are shown in figure 12, where the filled symbols represent values from equation (17) and the open symbols are from the sudden-freeze analysis. The curves are from the exact numerical solutions (with vibrational equilibrium) at two representative nozzle area ratios  $A/A^*$  and reservoir pressures  $p_0$ . The

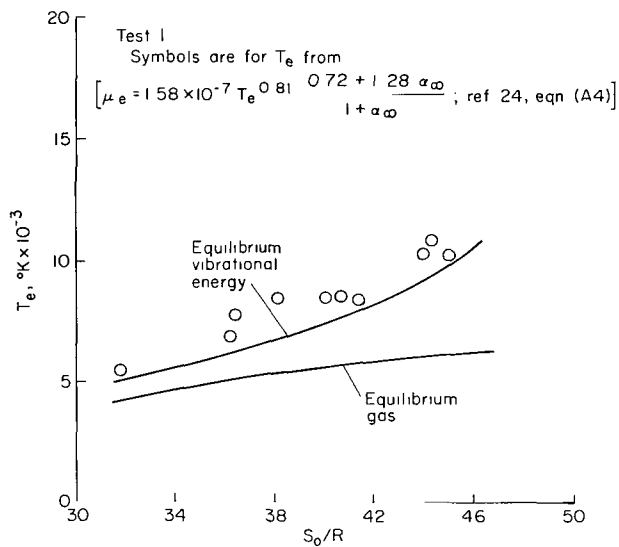


Figure 13.— Shock-layer temperature.

*Shock-layer Reynolds number*— Reynolds numbers in the stagnation-region shock layer were obtained from equation (14) and are listed in table 4. They remain fairly constant over the operating range, varying from 4.2 to 6.9/cm, as a result of the relatively small changes in density and viscosity observed earlier. These low Reynolds numbers reflect the high viscosities in the frozen shock layers of the present experiments.

*Mach number, Reynolds number, and A/A\**— The sudden-freeze method was used to evaluate the additional flow quantities, free-stream Mach number, Reynolds number, and effective area ratio. Results are listed in tables 4 and 5. For the smaller throat size (0.32 cm) the  $M_\infty$  increased with total enthalpy from 20 to 32 and for the 1.27-cm throat from 14 to 23. The Reynolds number did not vary in

a consistent manner with increasing enthalpy, apparently because of the increase in freeze Mach number (see fig. 11); values between 200 and 1000/cm were obtained. A substantial difference was observed, at intermediate enthalpies, between the Reynolds numbers for frozen and equilibrium vibrations (see table 5). Thus, a knowledge of the vibrational energy distribution is important in evaluating the properties of nonequilibrium streams at these energy levels.

The effective area ratio of the test stream comes directly from the sudden-freeze analysis, as shown in reference 6. The ratio  $A/A^*$  decreased with increasing reservoir enthalpy from 12,000 to about 9,000 with the small nozzle throat and from about 3,300 to 2,300 with the large throat. (The corresponding geometric area ratios are 56,000 and 3,600.) Representative boundary-layer displacement thicknesses  $\delta^*$  at the nozzle exit are listed in the last column of table 5. The very substantial 20- to 23-cm thicknesses that occur with the small nozzle throat correspond to the small inviscid core size noted earlier. Obviously, for the present reservoir pressure, 0.32 cm is about the smallest throat diameter that can be used in this nozzle.

## CONCLUDING REMARKS

The operating characteristics of an electric-arc-heated driver and shock-tube system, and the properties of high energy nitrogen flows expanded in a supersonic nozzle have been investigated. Driver temperatures up to 8000° K and pressures up to 340 atm were used to obtain tailored-interface conditions at shock Mach numbers from 7 to 19, enthalpies in the reflected-shock reservoir of test gas from 7 to 40 kJ/g, and test-section Mach numbers from 14 to 32. The gasdynamic processes in the shock tube and nozzle have been compared with theoretical, real-gas predictions. Local equilibrium conditions were assumed to exist everywhere in the shock tube; the nozzle flow was not so restricted, and substantial nonequilibrium effects were observed. The primary results of this investigation are summarized as follows.

1. The overall efficiency of the driver and shock-tube system was found to vary with the composition of the driver gas. Argon-helium mixtures were the most effective but did not give consistent shock-tube performance. Pure helium and pure nitrogen were less effective driver gases but produced more uniform results. Efficiencies from 40 to 100 percent were recorded.
2. An ideal, theoretical analysis of tailored-interface, shock-tube operation, which predicts a constant ratio of initial driver pressure to initial shock-tube pressure for tailoring at all shock velocities, was not confirmed by experiment. However, the nonideal effects that invalidated this prediction could be offset by increasing the pressure ratio, so that near-tailored operation was achieved for shock Mach numbers from 7 to 19.
3. Reflected shock relationships and a reservoir pressure history can be used to define reservoir conditions at total enthalpies between 7 and 40 kJ/g, if successive pressure changes are considered to be isentropic. There was no significant loss of energy from the reservoir gas during the 0.5- to 1.5-msec test period.
4. The proposed method of evaluating the properties of a nonequilibrium nozzle flow of nitrogen, using simultaneous measurements of stagnation heating rates (to noncatalytic surfaces) in three gasdynamic regimes, could not be fully utilized under current test-section conditions. Limitations on probe size prevented the attainment of an equilibrium boundary layer in the stagnation region. In future work, however, it may be possible to use a catalytic probe surface to recover the dissociation energy of the shock layer.
5. By combining elements of the three-probe diagnostic method with a sudden-freeze approximation of the flow behavior it is possible to define most of the properties needed for hypervelocity, gasdynamic studies in a nonequilibrium stream. This technique has been shown to give consistent results in a single-component gas (nitrogen) over a wide range of specific energies, with initial dissociation up to 75 percent.
6. Theoretical predictions were found to underestimate the energy retained in the inert degrees of freedom (dissociation and vibration) in a rapidly expanding stream of nitrogen. Typically, the flow departed from thermodynamic equilibrium just downstream of the nozzle throat and was effectively frozen at a local Mach number of about 2.

Ames Research Center

National Aeronautics and Space Administration  
Moffett Field, Calif., 94035, March 21, 1972

## REFERENCES

1. Wittliff, C. E.; Wilson, M. R.; and Hertzberg, A.: The Tailored-Interface Hypersonic Shock Tunnel. *J. Aerospace Sci.*, vol. 26, 1959, pp. 219-228.
2. Loubsky, W. J.; and Reller, J. O., Jr.: Analysis of Tailored-Interface Operation of Shock Tubes With Helium-Driven Planetary Gases. NASA TN D-3495, 1966.
3. Hertzberg, A.; Wittliff, C. E.; and Hall, J. G.: Development of the Shock Tunnel and Its Application to Hypersonic Flight. *ARS Progress in Astronautics and Rocketry; Hypersonic Flow Research*, F. R. Riddell, ed., Academic Press, Inc., vol. 7, 1962, pp. 701-758.
4. Nagamatsu, H. T.; and Martin, E. O.: Combustion Investigation in the Hypersonic Shock Tunnel Driver Section. *J. Appl. Phys.*, vol. 30, July 1959, pp. 1018-1021.
5. Mason, R. P.; and Reddy, N. M.: Combustion Studies in the UTIAS Hypersonic Shock Tunnel Driver. Proc. 5th Shock Tube Symposium, U. S. Naval Ordnance Laboratory, April 1965.
6. Hiers, R. S., Jr.; and Reller, J. O., Jr.: Analysis of Nonequilibrium Air Streams in the Ames 1-Foot Shock Tunnel. NASA TN D-4985, 1969.
7. Camm, J. C.; and Rose, P. M.: Electric Arc-Driven Shock Tube. *Phys. of Fluids*, May 1963, pp. 663-677.
8. Warren, W. R.; Rogers, D. A.; and Harris, C. J.: The Development of an Electrically Heated Shock Driven Test Facility. Second Symposium on Hypervelocity Techniques, Univ. of Denver, March 1962.
9. Lordi, J. A.; Mates, R. E.; and Moselle, J. R.: Computer Program for the Numerical Solution of Nonequilibrium Expansions of Reacting Gas Mixtures. NASA CR-742, 1966.
10. Reddy, N. M.: Shock-Tube Flow Analysis With a Dimensionless Velocity Number. NASA TN D-5518, 1969.
11. Glass, I. I.; and Hall, J. G.: Handbook of Supersonic Aerodynamics. Shock Tubes (Section 18). NAVORD Rep. 1488, vol. 6, Dec. 1959.
12. Flagg, R. F.: Detailed Analysis of Shock Tube Tailored Conditions. RAD-TM-63-64, AVCO Corp., Wilmington, Mass., Sept. 1963.
13. Reddy, N. M.: A Method for Measuring Reynolds Number, Viscosity, and Atom Concentration in Hypervelocity Nozzles. *AIAA J.*, vol. 6, July 1968, pp. 1398-1400.
14. Dannenberg, R. E.; and Silva, A. F.: Exploding Wire Initiation and Electrical Operation of a 40 kV System for Arc-Heated Drivers up to 10 Feet Long. NASA TN D-5126, 1969.

15. Dannenberg, R. E.; and Humphry, D. E.: Microsecond Response System for Measuring Shock Arrival by Changes in Stream Electrical Impedance in a Shock Tube. *Rev. Sci. Instru.*, vol. 39, Nov. 1968, pp. 1692-1696.
16. Reddy, N. M.: The Use of Self-Calibrating Catalytic Probes to Measure Free-Stream Atom Concentrations in a Hypersonic Flow. NASA CR-780, 1967.
17. Inger, G. R.: Nonequilibrium Stagnation Point Boundary Layers With Arbitrary Surface Catalycity. *AIAA J.*, vol. 1, 1963, pp. 1776-1784.
18. Seegmiller, H. L.; and Mazer, L.: A 500,000 Sample per Second Digital Recorder for the Ames Electric-Arc Shock Tunnel. IEEE Pub. 69 C 19-AES, 1969, pp. 243-247.
19. Potter, J. L.; and Bailey, A. B.: Pressures in the Stagnation Regions of Blunt Bodies in Rarefied Flow. *AIAA J.*, vol. 2, April 1964, pp. 743-745.
20. Dunn, M. G.: Application of Microwave and Optical Diagnostic Techniques in Shock-Tunnel Flows. AIAA Paper 68-394, 1968.
21. Hammit, A.: The Flow of a Dissociating Gas Around and Behind a Blunt Hypersonic Body. BSD-TDR-62-107, May 1962.
22. Pope, Ronald B.: Stagnation-Point Convective Heat Transfer in Frozen Boundary Layers. *AIAA J.*, vol. 6, no. 4, April 1968, pp. 619-626.
23. Lewis, C. H.; and Burgess, E. G., III: Charts of Normal Shock Wave Properties in Imperfect Nitrogen. AEDC-TDR-64-104, Arnold Engineering Development Center, Tenn., May 1964.
24. Okuno, A. F.; and Park, Chul: Stagnation-Point Heat Transfer Rate in Nitrogen Plasma Flows: Theory and Experiment. ASME Pub. 69-WA/HT-49, Nov. 1969.

TABLE 1.— RATIOS OF INITIAL DRIVER PRESSURE TO DRIVEN TUBE PRESSURE FOR TAILORED OPERATION

Driver/driven gases	He/N <sub>2</sub>	(0.3A + 0.7He)/N <sub>2</sub>	(0.4A + 0.6He)/N <sub>2</sub>	A/N <sub>2</sub>	N <sub>2</sub> /N <sub>2</sub>
$p_i/p_1$	117	31.5	25.5	11.7	25.0

TABLE 2.— SHOCK TUBE, NOZZLE RESERVOIR, AND TEST STREAM QUANTITIES FOR NITROGEN

1	2	3	4	5	6	7	8	9	10	11	12	13	14	
Test	$p_1 \times 10^3$ , atm	$M_s$	$p_{O'}$ , atm	$H_{O'}$ , kJ/g	$d^*$ , cm	$\zeta$ $p_t \times 10^3$ , atm	Theoretical	Measured	Local $p_t \times 10^3$ , atm	Measured	Measured $\dot{q}_{fm}$	Test interval	Test flow duration	
							$\dot{q}_{eq}$ W/cm <sup>2</sup>			$\dot{q}_{fr}$ W/cm <sup>2</sup>				
1 ↓	9.22	18.5	41.1	40.6	0.32	6.94	197	127	4.97	116	161	0.5	---	
			17.8	43.5	38.7		8.03	191	119	5.24	---	.6	---	
			17.7	39.1	38.5		7.21	181	123	4.62	120	153	.5	0.5
		13.2	16.0	40.8	30.6		6.12	142	---	6.12	119	165	.4	.4
			15.3	38.8	28.8		6.18	134	74	5.37	108	131	.4	.4
			14.9	38.1	27.0		5.71	124	68	5.71	---	136	.7	---
			13.0	35.4	21.6		5.30	100	58	5.30	91	125	.6	1.2
			11.4	39.5	17.9		5.24	83	55	5.24	83	108	.9	---
			11.3	34.7	17.1		4.56	75	49	4.56	79	108	.7	---
		26.3	6.9	19.4	6.9		2.58	22	18	2.58	28	40	1.2	1.6
	2 ↓	13.2	15.8	59.8	31.8		9.80	265	162				1.2	1.5
			13.2	13.7	42.5	24.4		6.73	177	111			1.2	1.7
			26.3	7.6	22.1	8.2		2.79	39	29			.9	1.3
		9.22	17.9	44.2	39.2	1.27	22.6	437	341			2.0	2.4	
		13.2	16.2	47.6	31.7		36.6	475	388			1.2	2.5	
			12.3	34.0	19.3		23.7	259	184			1.4	2.8	
			11.6	36.7	17.9		23.1	236	185			1.4	2.2	
		26.3	7.3	22.1	7.8		11.7	77	71			2.0	2.4	

TABLE 3.— EVALUATION OF STREAM TOTAL ENTHALPY, TEST 1

Measured $p_o$ , atm	Calculated $H_o$ , kJ/g	$\alpha_o$	Measured $\dot{q}_{fr}$ , W/cm <sup>2</sup>	Equivalent $\alpha_\infty$	Equivalent $(U_\infty)_{fr}$ , m/sec	Measured $\dot{q}_{fm}$ , W/cm <sup>2</sup>	Equivalent $(U_\infty)_{fm}$ , m/sec	$\frac{(U_\infty)_{fm}}{(U_\infty)_{fr}}$
41.1	40.6	0.74	127	0.57	6590	161	6430	0.977
43.5	38.7	.68	119	.58	6220	---	---	---
39.1	38.5	.69	123	.53	6480	153	6450	.996
40.8	30.6	.51	119	.50	5260	165	5310	1.008
38.8	28.8	.48	74	.47	5120	131	4800	.938
38.1	27.0	.44	68	.43	5030	136	4710	.937
35.4	21.6	.32	58	.30	4800	125	4650	.970
39.5	17.9	.22	55	.22	4590	108	4600	1.003
34.7	17.1	.20	49	.20	4560	108	4660	1.022
19.4	6.9	.02	18	0	3290	40	3160	.962

TABLE 4.— FLOW CONDITIONS AND TEST-SECTION FLOW PROPERTIES, TEST 1

$M_s$	$p_o$ , atm	$\xi$ $p_t \times 10^3$ , atm	$H_o$ , kJ/g	$S_o/R$	$\alpha_o$	$\alpha_\infty$	$\rho_\infty \times 10^5$ , kg/m <sup>3</sup>	$[Re/cm]_e$	$\mu_e \times 10^6$ , Nsec/m <sup>2</sup>	Sudden freeze			
										$A/A^*$	$M_\infty$	$[Re/cm]_\infty$	$\rho_\infty \times 10^5$ , kg/m <sup>3</sup>
18.5	41.1	6.94	40.6	45.1	0.74	0.57	1.78	4.49	2.61	8,900	29.8	289	2.27
17.8	43.5	8.03	38.7	44.1	.68	.58	2.10	4.98	2.61	8,600	31.8	328	2.59
17.7	39.1	7.21	38.5	44.4	.69	.53	1.74	4.17	2.70	9,000	29.3	233	2.20
16.0	40.8	6.12	30.6	41.5	.51	.50	2.25	5.54	2.19	9,700	32.2	446	2.58
15.3	38.8	6.18	28.8	40.8	.48	.47	2.40	5.68	2.20	9,500	30.1	436	2.92
14.9	38.1	5.71	27.0	40.2	.44	.43	2.29	5.32	2.15	10,000	29.4	370	2.45
13.0	35.4	5.30	21.6	38.2	.32	.30	2.33	5.71	2.03	10,300	25.0	318	2.67
11.4	39.5	5.24	17.9	36.5	.22	.22	2.51	6.30	1.85	11,800	24.5	318	2.93
11.3	34.7	4.56	17.1	36.3	.20	.20	2.23	6.30	1.64	11,800	24.0	266	2.78
6.9	19.4	2.58	6.9	31.8	.02	0	2.45	6.86	1.22	11,800	19.5	207	2.22

TABLE 5.— FLOW CONDITIONS AND TEST-SECTION FLOW PROPERTIES, TEST 2

$M_s$	$p_{O'}$ , atm	$d^*$ , cm	$p_t \times 10^3$ , atm	$H_{O'}$ , kJ/g	$S_{O'}/R$	$\alpha_o$	Theoretical E.B.L. <sup>a</sup> $\dot{q}_{eq}$ , W/cm <sup>2</sup>	Measured $\dot{q}$ , W/cm <sup>2</sup>	Theoretical F.B.L. <sup>b</sup> E.V. <sup>c</sup> $\dot{q}_{fr}$ , W/cm <sup>2</sup>	Theoretical F.B.L. <sup>b</sup> F.V. <sup>d</sup> $\dot{q}_{fr}$ , W/cm <sup>2</sup>	$\alpha_\infty$ E.V. <sup>c</sup> F.V. <sup>d</sup>	Sudden freeze approximation				
												A/A*	$[Re/cm]_\infty$	$M_\infty$	$\rho_\infty \times 10^5$ , kg/m <sup>3</sup>	$\delta^*$ , cm
15.8	59.8	0.32	9.80	31.8	41.3	0.53	309	162	158	157	0.50	8900	832	31.5	4.19	22.9
									173	171	.46	9600	640	29.6	3.94	22.4
13.7	42.5		6.74	24.4	39.0	.36	192	101	109	110	.33	---	---	---	---	---
									115	116	.27	11,000	303	24.0	2.78	21.3
7.6	22.1		2.79	8.2	32.4	.02	41.0	29.2	37.6	29.6	---	---	---	---	---	---
									.02	12,700	169	19.8	2.10	20.1		
17.9	44.2	1.27	22.5	39.3	44.4	.70	574	341	330	---	.56	3200	705	22.7	6.75	2.29
									346	---	---	---	---	---	---	
16.2	47.6		36.6	31.8	41.7	.53	590	388	377	---	.40	2250	452	17.5	12.4	8.14
									407	---	---	---	---	---		
12.3	34.0		23.7	19.3	37.4	.26	287	184	178	179	.25	---	---	---	---	---
									193	192	.19	2400	675	15.7	12.0	7.12
11.6	36.7		23.1	17.9	36.6	.22	261	185	178	179	.19	2600	981	17.0	13.6	5.84
									186	186	.13	2800	518	15.2	10.4	4.57
7.3	22.1		11.7	7.8	32.2	.02	80.6	71.1	80.6	71.0	.02	---	---	---	---	---
									0	3300	453	13.7	9.48	1.78		

<sup>a</sup>E.B.L. = equilibrium boundary layer

<sup>b</sup>F.B.L. = frozen boundary layer

<sup>c</sup>E.V. = equilibrium vibrations

<sup>d</sup>F.V. = frozen vibrations



021 001 C1 U 11 720609 SC0903DS  
DEPT OF THE AIR FORCE  
AF WEAPONS LAB (AFSC)  
TECH LIBRARY/WLOL/  
ATTN: E LOU BOWMAN, CHIEF  
KIRTLAND AFB NM 87117

POSTMASTER: If Undeliverable (Section 158  
Postal Manual) Do Not Return

*"The aeronautical and space activities of the United States shall be conducted so as to contribute . . . to the expansion of human knowledge of phenomena in the atmosphere and space. The Administration shall provide for the widest practicable and appropriate dissemination of information concerning its activities and the results thereof."*

— NATIONAL AERONAUTICS AND SPACE ACT OF 1958

## NASA SCIENTIFIC AND TECHNICAL PUBLICATIONS

**TECHNICAL REPORTS:** Scientific and technical information considered important, complete, and a lasting contribution to existing knowledge.

**TECHNICAL NOTES:** Information less broad in scope but nevertheless of importance as a contribution to existing knowledge.

**TECHNICAL MEMORANDUMS:** Information receiving limited distribution because of preliminary data, security classification, or other reasons.

**CONTRACTOR REPORTS:** Scientific and technical information generated under a NASA contract or grant and considered an important contribution to existing knowledge.

**TECHNICAL TRANSLATIONS:** Information published in a foreign language considered to merit NASA distribution in English.

**SPECIAL PUBLICATIONS:** Information derived from or of value to NASA activities. Publications include conference proceedings, monographs, data compilations, handbooks, sourcebooks, and special bibliographies.

**TECHNOLOGY UTILIZATION PUBLICATIONS:** Information on technology used by NASA that may be of particular interest in commercial and other non-aerospace applications. Publications include Tech Briefs, Technology Utilization Reports and Technology Surveys.

*Details on the availability of these publications may be obtained from:*

**SCIENTIFIC AND TECHNICAL INFORMATION OFFICE  
NATIONAL AERONAUTICS AND SPACE ADMINISTRATION  
Washington, D.C. 20546**